Ceramics International 43 (2017) 11722–11732

Contents lists available at ScienceDirect

Ceramics International

journal homepage: www.elsevier.com/locate/ceramint

N-doping $SrTiO_3$@$SrCO_3$ heterostructure electrode: Synthesis, electrochemical characterization, and varistor application

Marina Raschetti[a], Gabriela Byzynski[b,c,*], Caue Ribeiro[c], Elson Longo[d]

[a] Materials Engineering Department, Federal University of São Carlos, São Carlos, SP, Rodovia Washington Luís, Km 235, s/n - Jardim Guanabara, São Carlos , SP CEP: 13565-905, Brazil

[b] São Paulo State University (Unesp), Institute of Chemistry, Araraquara, Rua Prof. Francisco Degni, 55, Quitandinha, Araraquara, SP CEP: 14800-06, Brazil

[c] Embrapa Instrumentação, São Carlos, SP, Rua XV de Novembro, 1452, São Carlos, SP CEP: 13560-970, Brazil

[d] Chemistry Department, Federal University of São Carlos, São Carlos, SP, Rodovia Washington Luís, Km 235, s/n - Jardim Guanabara, São Carlos, SP CEP: 13565-90, Brazil

ARTICLE INFO

Keywords:
Composite electrodes
Photoelectrodes
$SrTiO_3$@$SrCO_3$
Characterization
Photocatalyst
Doping process

ABSTRACT

Optical traditional techniques, such as diffusive reflectance spectroscopy, are used to confirm absorption behavior modification after anion doping process. However, the doping process in some materials as a $SrTiO_3$ semiconductor was not clearly proved in different anions doping cases through traditional techniques. In this case, supporting technique as electrochemical measurements could prove a great help in elucidating the doping process modifications in the semiconductor material. In this paper, the electrochemical characterization was applied to analyze changes in energy bands produced by N-doping in $SrTiO_3$@$SrCO_3$ composite thin film electrodes. $SrTiO_3$@$SrCO_3$ and N-doped $SrTiO_3$@$SrCO_3$ nanoparticles were first characterized by X-ray diffraction to confirm a perovskite crystalline structure in both materials, whereas diffusive reflectance spectroscopy was used to demonstrate that no modification in the absorption spectrum is evident after doping. The thin films were observed by FESEM/SEM, and its deposition parameters were electrochemically evaluated. The electrochemical profiles of $SrTiO_3$@$SrCO_3$ and N doped $SrTiO_3$@$SrCO_3$ thin film electrodes were compared in dark and under UV-C light to determine the photocurrent. These measurements presented distinct results for the undoped and the doped materials, such as modification in photocurrent under UV-C illumination. $SrTiO_3$@$SrCO_3$ composite electrodes show important characteristics which could be classified as a potential candidate in varistor uses, especially in the low-voltage protection system. The presented results confirm that electrochemical methods are useful to analyze the synthesis efficiency to produce N-doped structures.

1. Introduction

Electron transfer caused by the absorption of a photon is the basis of photocatalysis in semiconductor materials. Highly reactive species, such as the hydroxyl radical, are produced by the electron transfer process and are responsible for driving various reactions, such as contaminant degradation. The semiconductor responds positively to illumination in a certain wavelength range, depending on its band-gap value [1].

Strontium titanate ($SrTiO_3$), a member of the perovskite oxide family, is one of the more commonly used semiconductors, due to its physical and chemical properties. It has a band-gap energy of 3.23 eV at 0 K, which permits good photoactivation in the ultraviolet (UV) light, but is limited for longer wavelength photons [2–4]. The doping process is commonly used to extend its absorption range to visible wavelengths. It has been shown that non-metallic dopants, such as N, C, and S, can reduce the $SrTiO_3$ band gap [3,5,6]. The dopant atoms create defects in the $SrTiO_3$ lattice, resulting in new energy levels located between the conduction and valence bands. Consequently, the band gap of semiconductor decreases and photocatalytic activity under visible light improves [5,7,8].

The efficiency of the doping process to produce N-doped $SrTiO_3$ is usually measured by X-ray diffraction (XRD) or diffuse reflectance spectroscopy (DRS). In the XRD spectra, a shift of diffraction peaks is expected, as the lattice parameters change on N-doping. In some cases, the diffraction peak corresponding to N-doped $SrTiO_3$ shifted to a higher angle, which indicates that the lattice constant decreased with nitrogen (N)-doping [4]. The variation of the diffraction peak is caused

* Corresponding author at: São Paulo State University (Unesp), Institute of Chemistry, Araraquara, Rua Prof. Francisco Degni, 55, Quitandinha, Araraquara, SP CEP: 14800-060, Brazil.

E-mail addresses: marina.raschetti@gmail.com (M. Raschetti), gabi.byzynski@gmail.com (G. Byzynski), caue.ribeiro@embrapa.br (C. Ribeiro), elson.liec@gmail.com (E. Longo).

http://dx.doi.org/10.1016/j.ceramint.2017.06.003
Received 5 May 2017; Received in revised form 25 May 2017; Accepted 2 June 2017
Available online 03 June 2017

by the formation of anion vacancies due to compound electroneutrality. DRS of N-doped $SrTiO_3$ shows that the N-doping induces a reduced electronic band gap and an enhanced light absorption [2,7]. Zhang *et al.* [5] reported the appearance of a band originating from N 2p electrons in the band gap of $SrTiO_3$, at a higher energy than the valence band and, in some cases, replacing the O 2p orbital band. However, some semiconductors do not present significant variation in traditional characterization techniques such as DRS.

Other way to expend the visible absorption characteristics of $SrTiO_3$ is to create heterostructures with coupling two different semiconductor material. Semiconductor heterostructures with diverse assemblies design have drawn an increased interest in recent years due to their application in different electrochemical devices as solar cells [9–11], photocatalytic systems [12–14], water splitting systems [15,16], sensor devices [17,18], and diodes [19]. The combination of two different semiconductors enables some advantages compared with only one material, as, for example, the oxidation and reduction steps process occurring in independent steps. A good chemical stability, abundance in nature, great solar spectrum absorption and defined conduction and valence band edges of the isolated semiconductor are important parameters to consider to choose an heterostructure [20]. $SrTiO_3$@TiO_2 heterostructure nanotubes array films obtained by hydrothermal method present an increase in light absorption and Fermi level effectively shift, promoting better charge transfer [21]. $SrTiO_3$@$SrCO_3$ heterostructure obtaining by solvothermal method shows efficient photocatalytic effect of methylene blue dye solar degradation.[22] and $SrTiO_3$@$SrCO_3$ obtaining by sol-gel method is and effective photocatalyst for methane photo-oxidation [23].

An alternative to probing band modifications as charge transfer when used doped or heterostructure semiconductor is analyzing the electrochemical properties of the materials. By the principles of these techniques, if modifications of electronic transport into the semiconductor were done, they should alter the global profile of an electrochemical measurement. However, the electrode preparation is not trivial, involving some steps to assure that the measurement reflects the real effect expected by the dopant; also, the interpretation of such results may be a challenge, depending on the applied conditions [24–26].

Then, the aim of this paper is to demonstrate the efficiency of the N-doping process by electrochemical methods, since the traditional characterization methods may not present any modification of behavior after doping. The $SrTiO_3$ nanoparticles were synthesized by a modified version of the polymeric precursor method proposed by Soares et al. [7] using polyvinyl alcohol instead of ethylene glycol. The N-doped $SrTiO_3$ nanoparticles were synthesized by the same method, adding urea as the nitrogen source in the resulting resin. A new and simple method to rapidly deposit thin film electrodes on indium tin oxide (ITO) is introduced, using of polyvinyl alcohol (PVA) as a polymeric precursor of $SrTiO_3$ resin. Both nanoparticles were characterized by XRD, DRS, and electrochemical methods, such as cyclic voltammetry, differential pulse voltammetry, and impedance spectroscopy, which present corroborative results to demonstrate that the doping process is efficient.

2. Materials and methods

2.1. $SrTiO_3$ nanoparticles synthesis

Separated solutions of titanium isopropoxide in citric acid with a molar ratio of 1:3, and of strontium carbonate in citric acid with a molar ratio of 1:1.5 were prepared [27]. After complete dissolution and homogenization by magnetic stirring at 90 °C, the titanium and strontium solutions were mixed with a 1:1 M ratio of titanium and strontium. As citric acid promotes the complexation of Ti^{4+} and Sr^{2+}, the reaction between metal precursors (titanium isopropoxide ($Ti[(CH_3)_2O]_4$) and strontium carbonate ($SrCO_3$)) with citric acid, generate titanium citrate and strontium citrate, with an excess of carbon species dissolved in solution. The excess of carbon species in solution could influence the complexation equilibrium of strontium carbonate, promoting a decrease in $SrCO_3$ complexation and promoting the permanence of carbonate in the heterostructure.

Finally, a solution of polyvinyl alcohol (PVA) was added, to a molar ratio of 1:1 between citric acid and PVA. The resulting resin was stirred at 90 °C until completely homogenized, and the required viscosity was controlled by the water content. The N-doped resin $SrTiO_3$@$SrCO_3$ resin was obtained, following the same steps, by adding urea in the $SrTiO_3$@$SrCO_3$ resin, in a ratio 2% (w/w), in order to achieve 2% of nitrogen doping level. Doping process generally uses low content of dopant element, in this case, N content, and urea is a good candidate to use as N-source [28–30]. The resins and electrodes were first annealed at 100 °C (2 h) and 150 °C (2 h), respectively, in a conventional electric oven to promote water and solvent evaporation. The resulting amorphous powders and films were later crystallized at 650 °C, for 6 h.

2.2. Thin film deposition for electrode elaboration

The use of thin film photoelectrode is limited to the deposition technique of semiconductor solution on a conductive substrate. In liquid coating techniques, the spin-coating is commonly used for laboratory-scale devices due to its simplicity and high reproducibility. A uniform thin film is then produced after the spin-off and solvent evaporation, which requires a thermal treatment. One suitable way to enable a fast thin-film drying during the spin-coating deposition, by using an appropriated semiconductor viscosity solution, could be produced to save time and it allows several subsequent layer depositions. As a result, the deposited electrode is annealed and crystallized after only the deposition of all layers, providing a better homogeneity at the substrate surface.

ITO was used as a conductor substrate for electrode elaboration. Thin films of $SrTiO_3$@$SrCO_3$ or N-doped $SrTiO_3$@$SrCO_3$, composed of up to 5 layers, were deposited by spin-coating. Each layer was deposited by a 100-μL drop of resin on the substrate, and a program of rotation at 500 rpm, then 3500 rpm for 30-s periods each. This spin-coating program dried the films reasonably, enabling the sequential deposition of 5 layers. The deposited electrode area was controlled during deposition by masking parts of the ITO with removable Teflon tape to facilitate electrochemical measurements. The deposited areas varied between 20 and 80 mm^2.

2.3. Characterization

The $SrTiO_3$@$SrCO_3$ and N-doped $SrTiO_3$@$SrCO_3$ nanopowders were first characterized by XRD (Shimadzu XDR 6000). The spectra were collected with a Cu ($\lambda_{Cu\text{-}K\alpha}$ = 0.154 nm) anode, from 2θ = 10–80°, at 2° min^{-1}.

Diffuse reflectance UV–vis spectra were obtained by using an ultraviolet–visible–near infrared (UV–vis–NIR) Cary 5 G spectrophotometer. Before each measurement, the substrate spectrum was recorded for baseline correction. UV–vis spectra were recorded in the diffuse reflectance mode and transformed to a magnitude proportional to the extinction coefficient (K) through the Kubelka–Munk model. The equation is a function of the extinction coefficient and the scattering (S) with the reflectance (R). For comparison, all spectra were arbitrarily normalized to an intensity of 1.0.

$$\frac{K}{S} = \frac{(1-R)^2}{2R} \equiv F(R_\infty) \quad (1)$$

The sample morphologies were observed by scanning electron microscopy (SEM) (Zeiss FE-SEM Supra 35) and field emission scanning electron microscopy (FESEM) (JSM-6701F/JEOL). Energy Dispersive X-ray spectroscopy -_EDX (Zeiss FE-SEM Supra 35) was used by analyzed the constituent elements of the samples. Atomic force microscopy was used to analyze the topography of the electrode

(Dimension V (Veeco) AFM), using a cantilever with a spring constant of 0.03 N m^{-1}, in contact mode at a scan rate of 1 Hz.

The nitrogen doping level as $SrCO_3$ percentage in heterostructure were confirmed by X-ray photoelectron spectroscopy (XPS) (Thermo K-Alpha XPS _Thermo Scientific, Inc.) with radiation of Al K under vacuum condition < 10^{-8} bar and spot size of 400 µm. The Survey spectrum resolution was 1 eV with 5 scans, and the high-resolution spectrum was 0.1 eV with 50 scans. CasaXPS software was used for data treatment.

Photoelectrochemical measurements were carried out in a conventional three-electrode system, connected to a computer-controlled potentiostat (AUTOLAB PGSTAT® 30). The three-electrode system contained a photoelectrode as the working electrode, a Pt wire as the counter electrode, and a Saturated Calomel Electrode (SCE) as the reference electrode. The $SrTiO_3$ electrodes have different numbers of layers and deposited areas, which are always specified. Firstly, a conditioning potential of 2 V was applied to clean the photoelectrode surface. Cyclic voltammograms were measured in a 0.05 mol L^{-1} aqueous solution of potassium ferricyanide ($K_3Fe(CN)_6$)(Merck) at 20 mV s^{-1}, with a potential range of −0.5–2 V vs. SCE. Every measurement was repeated 5 times, to ensure equilibrium. In the results, only the fifth voltammogram is presented for every measurement. Differential pulse voltammograms were measured in a basic solution of potassium sulfate (K_2SO_4) (0.15 mol L^{-1}) and sodium sulfide ($Na_2S\cdot 9H_2O$) (0.45 mol L^{-1}) with a pH of 12.7, between −0.5 and 1 V vs. SCE, in the dark and under ultraviolet-C (UV-C) light.

3. Results and discussion

3.1. Powder characterization

Fig. 1 shows the XRD patterns of $SrTiO_3$@$SrCO_3$ and N-doped $SrTiO_3$@$SrCO_3$ nanoparticles synthesized by the polymeric precursor method. The main peaks in the 2θ patterns, identified by (*), at about 23°, 32°, 40°, 46°, 52°, 58°, 68°, and 78°, can be attributed, respectively, to the (100), (110), (111), (200), (210), (211), (220), and (310) planes of the perovskite cubic structure of $SrTiO_3$ (JCPDS 35–0734) [6]. It should be noted that some $SrCO_3$ diffraction peaks, identified by (°), are present at low intensity (JCPDS 05–0418), due to the precursors of $SrTiO_3$ synthesis. In this way, it is possible to classify the resulted material as a composite material, indicated by $SrTiO_3$@$SrCO_3$. The doping process does not modify any crystallographic structure neither the molecular composition.

The DRS spectra of $SrTiO_3$@$SrCO_3$ and N doped $SrTiO_3$@$SrCO_3$ are presented in Fig. 2A, where an increase in absorption at around

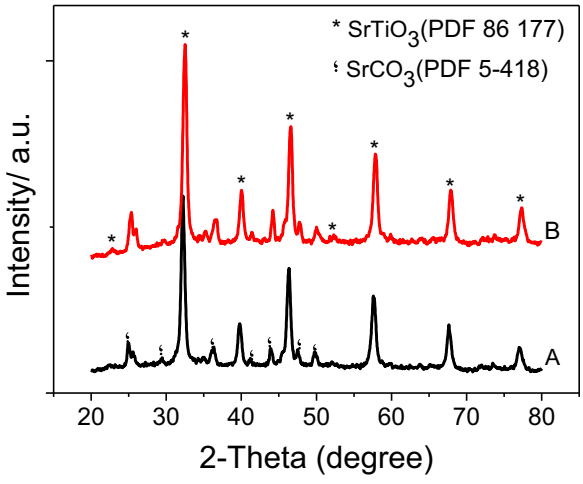

Fig. 1. X-ray diffraction patterns of (A) $SrTiO_3$@$SrCO_3$ and (B) N doped $SrTiO_3$@$SrCO_3$ powders.

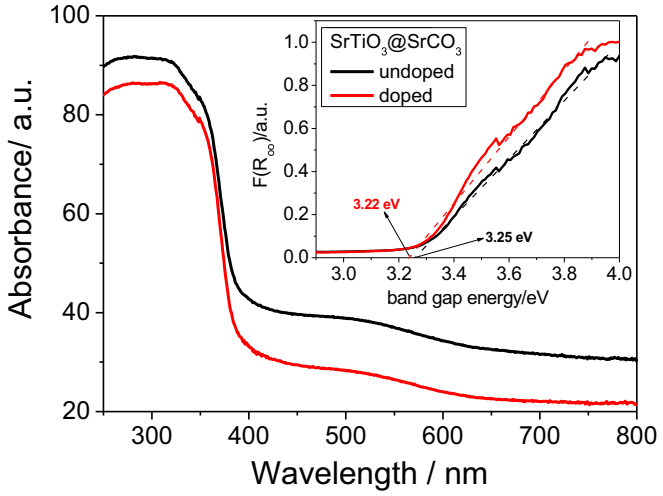

Fig. 2. DRS spectra of $SrTiO_3$@$SrCO_3$ and N doped $SrTiO_3$@$SrCO_3$ powders. (insert) Band gap determination by Tauc equation.

375 nm is evident in both samples. The band gap was determined by the Tauc equation (Fig. 2B). The band gap value obtained for $SrTiO_3$@$SrCO_3$ compose (3.25 eV) nanoparticles is similar to the $SrTiO_3$ reported value (3.23 eV) [[6,31,32], which confirms the synthesis of $SrTiO_3$ by the method presented. The N-doped $SrTiO_3$@$SrCO_3$ heterostructure presents a similar band gap value (3.22 eV). However, the small difference in the band gap value could disfeature the real absorption distinction (Fig. 2A). Then, the presence of N atoms creates two possible situation: oxygen vacancies (defects) and distortion in the crystalline structure of $SrTiO_3$, due to the atomic radii size difference between N and O, resulting in a shift of the absorption behavior. It is well known that doping with N and Fe decreases the $SrTiO_3$ band-gap value [31,33–35]. However, in the case of N, Nuraje et al. [33] doped $SrTiO_3$ particles by N-flux calcination and noticed no variation of absorption in the visible region. On the other hand, Liao et al. [36] confirmed that the N 2p orbital has a minor interference in substitutional doping of the O 2p orbital, but could significantly contribute to N-doped $SrTiO_3$@$SrCO_3$ photocatalytic activity in the visible region.

XPS spectra were obtained (Fig. 3) with powders samples to confirm the doping process over $SrTiO_3$@$SrCO_3$ composite semiconductor, the amount of nitrogen in $SrTiO_3$ and the difference in the oxidative state of C1s, O1s, Sr 3d, and Ti 2p after the doping process. The composite structure of $SrTiO_3$ and $SrCO_3$ will confirm trough the C 1 s high-resolution spectra (Fig. 3A), in which the presence of two main binding energy peaks was noticed. The peak with higher binding energy corresponds to carbon contamination due to samples exposition to the atmosphere (~284.0 eV for both samples, undoped and doped one). The second binding energy peaks are related to carbonate component (O-C=O) in $SrTiO_3$@$SrCO_3$ (287.41 eV) and N-doped $SrTiO_3$@$SrCO_3$ (288.45 eV), which confirms the $SrCO_3$ presence. For N 1 s high-resolution spectra of $SrTiO_3$@$SrCO_3$ and N doped $SrTiO_3$@$SrCO_3$ samples (Fig. 3B), the incorporation of N is confirmed in $SrTiO_3$ lattice due to the peak in 399.73, which is present in N-doped $SrTiO_3$@$SrCO_3$ and absent in $SrTiO_3$@$SrCO_3$ high-resolution spectra. The amount of N in $SrTiO_3$@$SrCO_3$ is restricted by a low concentration of oxygen vacancies in the pristine sample. [37]. The N insertion on the composite caused a shift in carbonate component in C 1 s high-resolution spectra (Fig. 3A), probably due to the oxygen vacancy availability. N compound presence promotes the binding between $SrTiO_3$ and $SrCO_3$, due to charge compensation, increasing the $SrCO_3$ content in N-doping $SrTiO_3$@$SrCO_3$ sample and, consequently, the interface interaction between $SrCO_3$ and $SrTiO_3$. Similar results are possible to observer for doping $SrTiO_3$ material with fluorine and nitrogen. When fluorine is introduced in semiconductor structure, a higher N content is accepted for the $SrTiO_3$, due to the charge

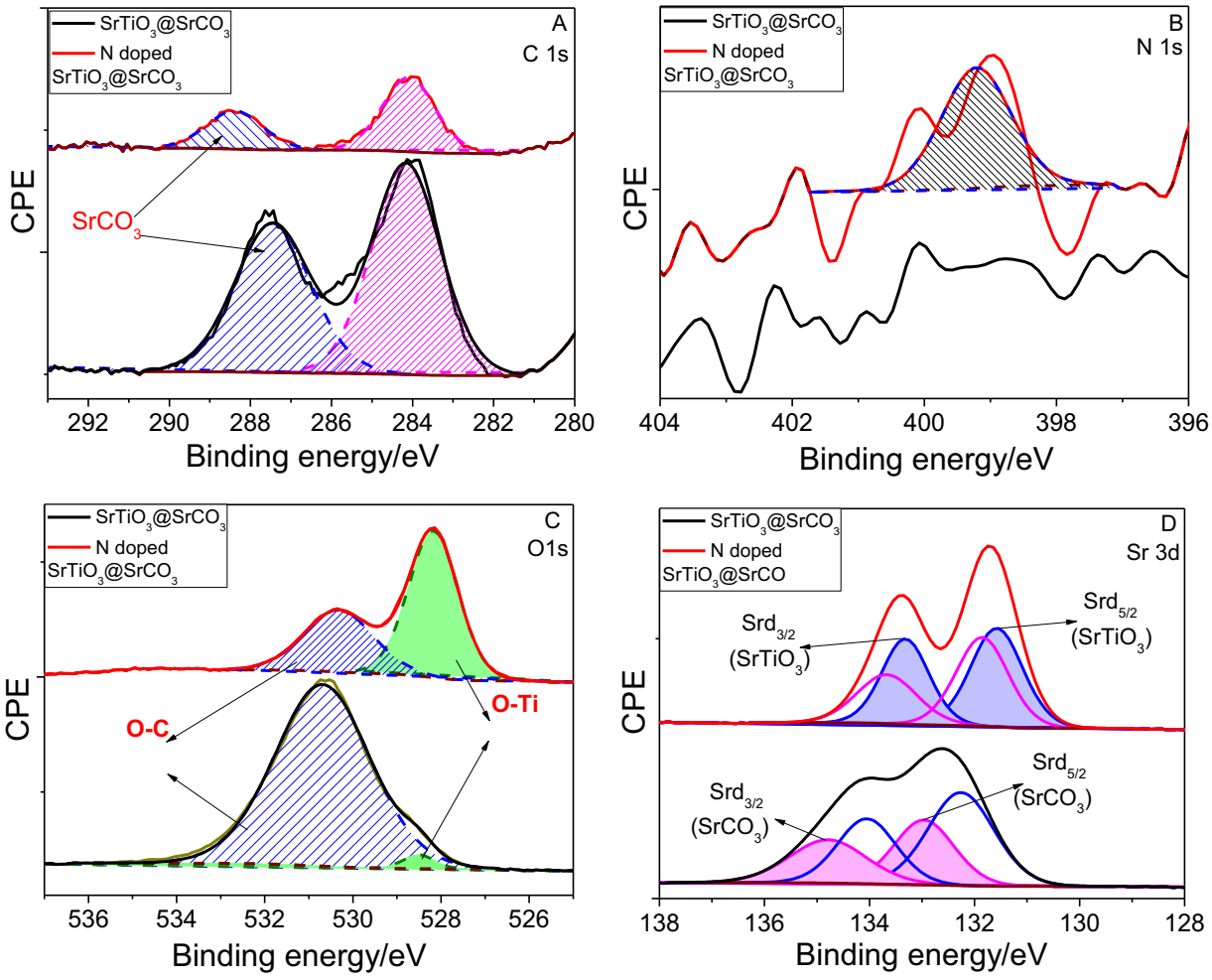

Fig. 3. XPS spectra of C1 s core level (A), N 1 s core level (B), O 1 s core level (C), and Sr 3d core level (D) obtained from $SrTiO_3$@$SrCO_3$ and N doped $SrTiO_3$@$SrCO_3$.

copensation [38]. The same occurs with lanthnum (La) co-doped N-$SrTiO_3$ [39]. Besides the differences in C 1 s and N 1 s, the Ti 2p (Fig. SI) spectra do not suffer any oxidative state alteration with N-doping and confirm the $SrTiO_3$@$SrCO_3$ heterostructure creation [37,40].

The O 1 s asymmetric peaks can be deconvoluted, for both samples (Fig. 3C), into two components with lower (528.48 and 528.17 eV for $SrTiO_3$@$SrCO_3$ and N-doped $SrTiO_3$@$SrCO_3$, respectively) and in higher binding energy (530.66 for $SrTiO_3$@$SrCO_3$ and 530.35 eV for N-doped $SrTiO_3$@$SrCO_3$). The first one, in lower binding energy, corresponds to O binding to Ti (O-Ti), whereas the other, in higher binding energy, is referred to O bonded with C (O-C). After N doping, the binding energy peaks shift, suggesting that the N doping will suppress the O vacancy formation in $SrTiO_3$, probably caused by N presence.

The Sr 3d high-resolution spectra (Fig. 3D) confirms the distortion in the $SrTiO_3$@$SrCO_3$ crystalline structure after N doping. Sr 3d region has well resolved spin-orbit component with multiple Sr chemical states. For both samples, $SrTiO_3$@$SrCO_3$ and doped one, the spin-orbit related to Sr chemically bound to Ti and O ($SrTiO_3$) are representing by blue peaks in Fig. 3D, presenting binding energies of 132.26 and 134.05 eV for $SrTiO_3$@$SrCO_3$, and 131.57 and 133.32 eV for N-doped $SrTiO_3$@$SrCO_3$. The pink peaks in Fig. 3D are related to Sr bonded to C and O ($SrCO_3$) with binding energies of 132.96 and 134.79 eV for $SrTiO_3$@$SrCO_3$, and 131.85 and 133.67 eV for doped $SrTiO_3$@$SrCO_3$. Another evidence of N doping is the shift caused by the binding energy of Sr 3d peaks, similar as occurs in O spectra. The N content is sufficient to accommodate in oxygen vacancies, and the modification absorption behavior, presented by DRS, could be confirmed to the distortion of $SrTiO_3$ lattice caused by N insertion than the creation of more oxygen vacancies.

Trough the spin-orbital quantification peaks of Sr 3d and the composition of samples obtained by XPS analysis, the $SrCO_3$ content of each sample is obtained. In the case of Sr 3d and Ti 2p spectra, the higher binding energy peaks of the spin-orbital were used to quantification measureaments. Table 1 indicates the content of C, O, N, Sr, and Ti in samples with the main binding energy peaks for elements and, the content of Sr 3d spin orbital peaks could estimate the $SrCO_3$ percentage in heterostructure as 5.99% for $SrTiO_3$@$SrCO_3$ and 8.89% for N-doped $SrTiO_3$@$SrCO_3$.

Table 1
Elements constitution of samples $SrTiO_3$@$SrCO_3$ and N-doped $SrTiO_3$@$SrCO_3$ obtained by XPS analysis.

	$SrTiO_3$@$SrCO_3$		***N-doped $SrTiO_3$@$SrCO_3$***	
	Position (eV)	**Content (%)**	**Position (eV)**	**Content (%)**
C 1 s	284.16	23.00	284.09	11.08
	287.45	18.06	288.39	6.09
O 1 s	528.50	1.16	528.17	34.32
	530.69	45.83	530.32	20.10
Ti $2p^{3/2}$	457.41	2.16	457.06	11.46
Sr $3d^{5/2}$	132.26	5.99	131.57	8.89
	132.96	3.79	131.85	8.02
N 1 s			399.21	0,04

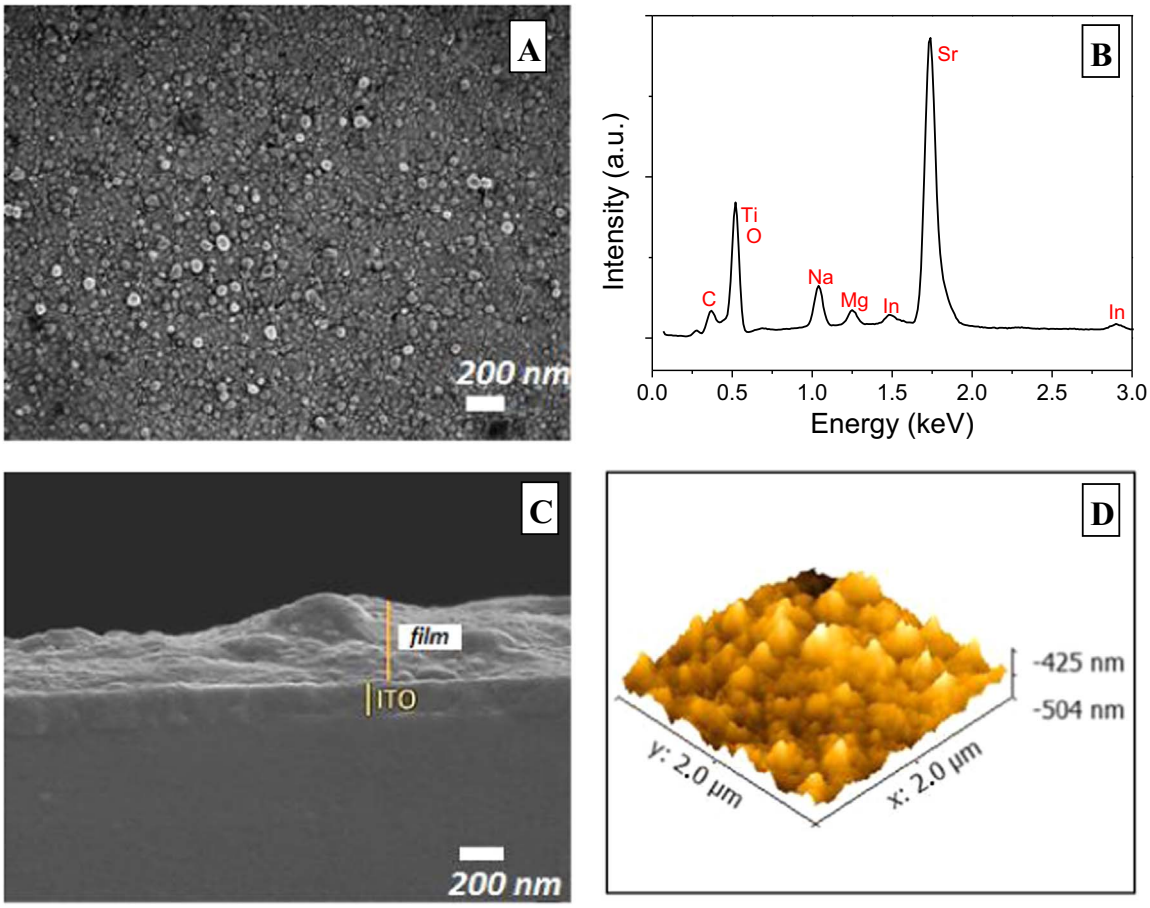

Fig. 4. (A) FESEM image of $SrTiO_3$@$SrCO_3$ thin film topology. (B) EDX spectra of $SrTiO_3$@$SrCO_3$ thin film topology (C) FESEM/SEM image of the fracture of a $SrTiO_3$@$SrCO_3$ thin film, deposited on ITO (D) AFM image of $SrTiO_3$@$SrCO_3$ thin film electrode.

3.2. Thin film electrode characterization

The SEM images (Fig. 4A) display the thin film structure deposited on the ITO substrate. Structural defects are observed on the thin film surface, due perhaps to the temperature treatment. However, these defects do not influence the electrochemical response of the thin films, as presented below. Similar film structures were observed for SnO_2–TiO_2 thin films obtained by the sol-gel method [41]. Fig. 4B confirms the results presented by XPS powders samples, in which C, Ti, Sr, and O are presented in EDX spectra of the $SrTiO_3$@$SrCO_3$ electrode. The composition of the sample also show the presence of some impurities as Na, Mg and In, probably due to the microscope electrode sample preparation.

A fracture of the $SrTiO_3$@$SrCO_3$ thin film was observed by FESEM/SEM (Fig. 4C). While the ITO thickness is constant across the substrate, the $SrTiO_3$@$SrCO_3$ thin film has a variable thickness due to the centrifugal force of the deposition method (spin-coating). The FESEM/SEM image shows roughness film with thickness obtained at the ITO edges about 300 nm. AFM image (Fig. 4D) of $SrTiO_3$@$SrCO_3$ electrode present continuous film electrode, without phase separation, and confirms the film rugoses characteristics observed in FESEM/SEM images. The thickness of the $SrTiO_3$@$SrCO_3$ film electrode varies from 425 to 504 nm.

The voltammetric response of the $SrTiO_3$@$SrCO_3$ thin film electrode was initially evaluated with cyclic voltammetry, Fig. 5, which was performed with a usual and common electrolyte used for characterization principles ($K_3Fe(CN)_6$ solution (0.05 mol L^{-1})) and a reference electrode as SCE. First, cyclic voltammograms of $SrTiO_3$@$SrCO_3$ thin film electrodes with 20 mm^2 as geometric area and with 1, 3, and 5 layers deposited by spin-coating onto an ITO substrate were compared, as shown in Fig. 5A. The experiment was performed at a scan rate of 20 mV s^{-1}, using a Pt counter electrode. A bare ITO substrate was analyzed for comparison. Well-defined cathodic (+0.32 V vs. SCE) and anodic peaks (+0.82 V vs. SCE) are present when analyzing $SrTiO_3$@$SrCO_3$ electrodes, as illustrate in Fig. 5A, whereas on the ITO substrate electrode the reduction process exhibits lower voltammetric intensities. Both redox peaks are correlated with the reduction and oxidation reaction of the ions $Fe(CN)_6^{-3/-4}$, showing similarity with previous reported [27,42,43]. The oxidation and the reduction currents increase linearly with the number of layers deposited in this condition (20 mV s^{-1}). This linearity did not occur at the higher scan rates (50 and 100 mV s^{-1}, figures not presented here), as equilibrium is not reached. The best response for a $SrTiO_3$@$SrCO_3$ electrode with 5 layers suggests a favorable interaction between the ions $Fe(CN)_6^{-3/-4}$. Even the concentration of $SrTiO_3$@$SrCO_3$ semiconductor nanoparticles increases in the electrode as layer number increases, the $SrTiO_3$@$SrCO_3$ thin film electrode with 5 layers deposited on ITO indicates a more effective electron transfer process.

The current ratio (anodic current peak/cathodic current peak, $I_{p,a}/I_{p,c}$), another important parameter for characterization analysis of electrode surface voltammetric responses, is determined and presented in Fig. 5B. For a reversible voltammetric process occurs on the electrode surface, the $I_{p,a}/I_{p,c}$ should present a value of 1.0 and the process is diffusion controlled [44]. As the results presented in Fig. 5B demonstrate, the electrode process studied cannot be considered totally reversible, since the anodic currents are more elevated than cathodic currents, and the estimated ratio of $I_{p,a}/I_{p,c}$ is greater than one at all conditions. Another evidence that confirms the quasi-reversibility of the voltammetric process is the potential values of peak-to-peak separations (ΔE). As for the reversible process, the ΔE should be 57/

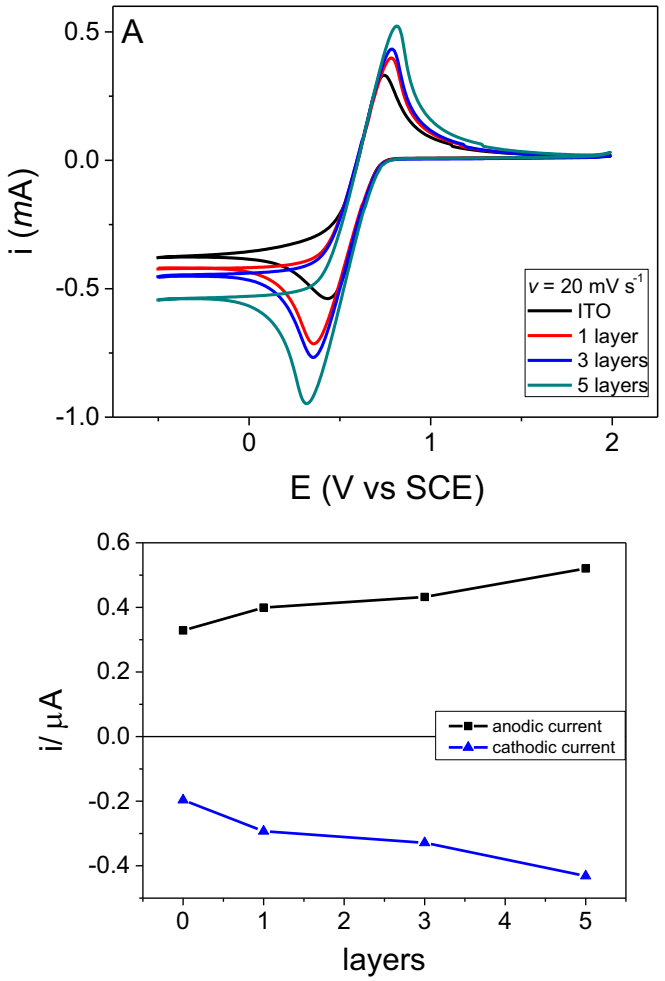

Fig. 5. (A) Cyclic voltammetry of $SrTiO_3$@$SrCO_3$ electrodes of 1, 3 and 5 layers and their substrate (ITO), with a Pt counter electrode, in $K_3Fe(CN)_6$ (0.05 mol L^{-1}) at a scan speed of 20 mV s^{-1}; geometric area of 20 mm^2. (B) Linear relation between the main peak intensity and electrode number of layers, for both oxidation and reduction peaks.

n mV, which n is the number of electrons participating in the redox reaction. Considering only one electron in redox reaction of ions $Fe(CN)_6^{-3/-4}$, the ΔE obtained in voltammograms in Fig. 5A is clearly different from 57 mV, confirming the quasi-reversibility redox process [44].

In the quasi-reversible process, the mass transport in electrode surface is governed by a mixed-control regime, which both, diffusion of reduced and/or oxidized species and electron transfer occurs [45]. These results are by thin film electrode characteristic, as presented in semiconductor nanoparticles and may influence in kinetic of electron transfer of electrode to solution species. Mass transport governed by the diffusion of reduced and/or oxidized species in only influenced by the time consumed by such species reach the electrode surface, adsorb and then diffuse to bulk solution. In this case, the electron transfer at electrode surface occurs rapidly, and the process is considered reversible. In the mixed-control regime, the electron transfer route at electrode surface spend more time to happen, characterizing the quasi-reversible reaction behavior [27,43,46].

3.3. The rate of electron transfer (k_s)

Cyclic voltammograms were evaluated at different scan rates (υ = 10–150 mV s^{-1}) to determine the characteristic process that occurs at the electrode/solution interface (Fig. 6A). The oxidation peak potential shifts to a more positive value and the redox peak potential change negatively. It can be seen that the peak current for the current response in the forward and backward direction increases as the scan rate increases. The dependence of the peak current on scan rate follows a characteristic square root law for reversible cyclic voltammograms described by Randles-Sevcik equation. The same equation could be used for irreversible and quasi-reversible electrochemical responses in a different way, using a correction factor of $0.496(\alpha)^{0.5}/0.446$. The correction factor value is 0.7869, assuming α = 0.5, and the Randles-Sevcik equation for the quasi-reversible and irreversible process is expressed as [44,45,47]:

$$I_O = -0.496\sqrt{\alpha n'}\,nFA[C]_{bulk}\sqrt{\frac{FvD}{RT}}$$

where I_o is the peak current (A), A is the electrode area (cm^2) n is the overall electrons transferred during the process per molecule diffusing to the electrode surface, [C] is the concentration of species in the bulk solution ($mol{\cdot}cm^{-3}$), F is the Faraday constant, T is temperature (K), R is the gas constant, ν is the scan rate (V s^{-1}), and D is the diffusion coefficient ($cm^2{\cdot}s^{-1}$). Note the n' denotes the number of electrons transferred in the rate-determining reaction step, the dependence of the peak current, which implies a non-linear increase for the case of n electrons, transferred simultaneously.

The relation between current density and $\nu^{0.5}$ is presented in Fig. 6B. In the potential range of 10–150 mV s^{-1}, both redox peaks display an increase almost linearly correlated to $\nu^{0.5}$, as confirmed by the R^2 value of their linear fits. The near-linearity is indicative that the system can be classified as quasi-reversible, based on the characteristics of reversibility discussed above. Assuming that the number of electrons transferred in redox reactions is one, the values of D obtained by the slopes of Fig. 6B (D_{ox} 6.55 × 10^{-1} $cm^2{\cdot}s^{-1}$ and D_{red} 6.17 × 10^{-1} $cm^2{\cdot}s^{-1}$) also confirm the quasi-reversibility of the system.

The k_s is defined as the speed of electron transfer between the redox reagent and the electrode surface and is considering restricted and determinate by the rate of electron exchange at the electrode/redox active reagent interface. The Butler-Volmer equation defines k_s relation (in m s^{-1}) with electrode area A, the transfer coefficient α, the overpotential η, and Faraday constant F. Considering a process as $A + ne^- \rightarrow B$, and the equilibrium conditions, the Butler-Volmer equation is [44]:

$$I_o = nFAk_s[A]_{bulk}^{-\alpha}[B]_{bulk}^{\alpha}$$

The ΔE experimentally determination in Fig. 6A may be used directly. As recognized α = 0.5 and D values, for the determination of the k_s for heterogeneous electron transfer as a function of temperature and scan rate υ, by the slope of Log υ vs. ΔE relation (Fig. 6C), based on the equation above [44]:

$$\log\left(k_s\sqrt{\frac{RT}{nF\upsilon D}}\right) = 0.294\left(\frac{nF}{RT}\Delta E - 2.218\right)^{-1} - 0.0803 - 0.108\left(\frac{nF}{RT}\Delta E - 2.218\right)$$

The k_s obtained by the slope of Fig. 6C (42.65 m s^{-1}) should be divided by log $\sqrt{(D)}^{-1}$ to obtain the rate of the electron transfer for anodic and cathodic current. For the case of the quasi-reversible reaction of ions $Fe(CN)_6^{-3/-4}$, both rates of electron transfer shown slightly different values. For anodic current, the rate obtained was 464.24 m s^{-1} and for the cathodic condition, the rate obtained was 406.77 m s^{-1}, confirming the quasi-reversibility of electrochemistry reaction.

3.4. Electrochemical process model

The Nyquist plot was used to model the electrochemical processes of electron transfer involved in the electrode/solution system, using the association of different electric circuit elements. Fig. 7 shows the

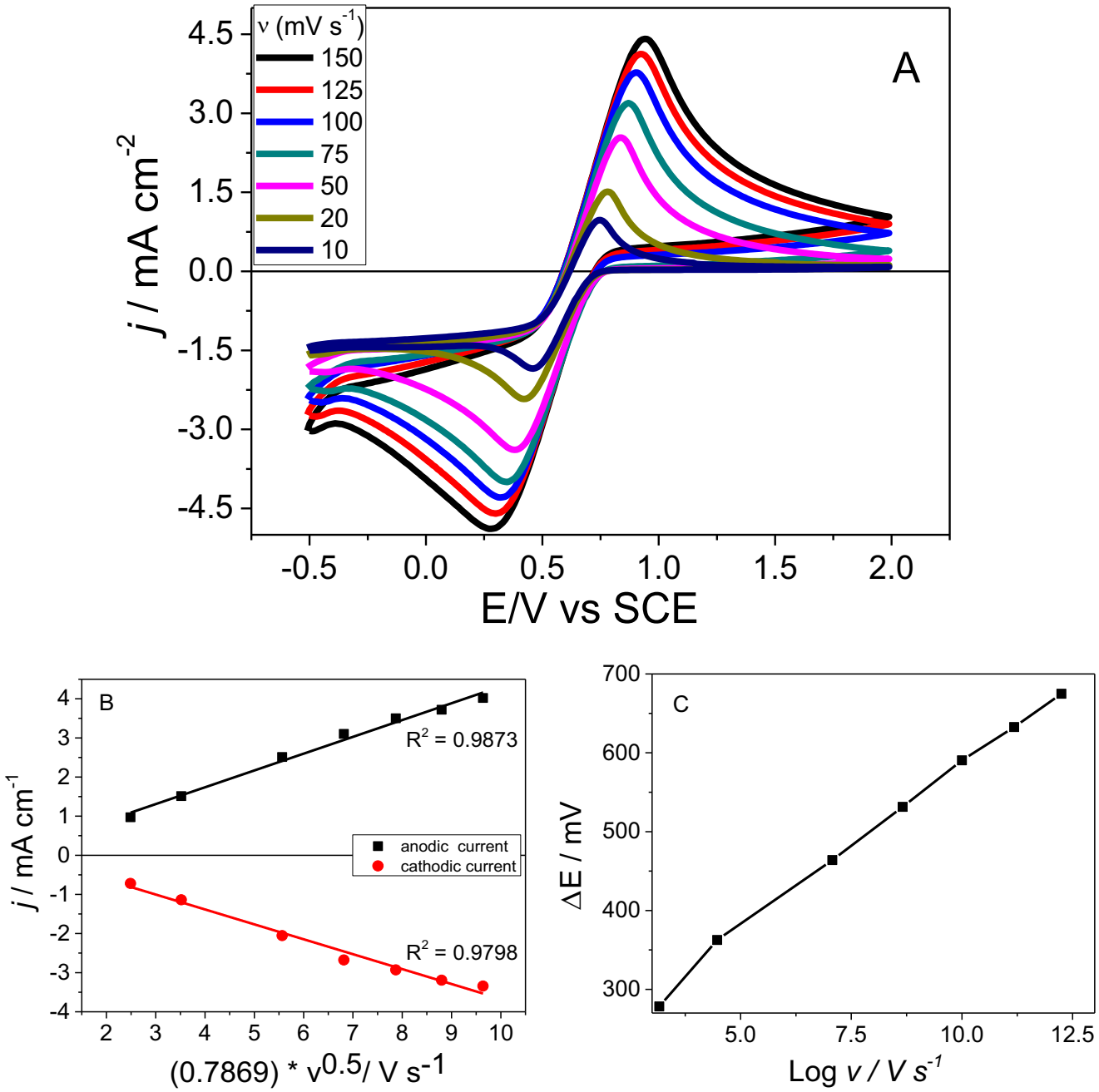

Fig. 6. (A) Cyclic voltammetry of $SrTiO_3$@$SrCO_3$ electrode of 40 mm² with 5 deposited layers, with a Pt counter electrode, in $K_3Fe(CN)_6$ (0.05 mol L^{-1}), under different scan rates; (B) Linear relation between the main peak intensity and scan rate, for both oxidation and reduction peaks (C) Relation between the peak-to-peak potential (ΔE) and Log scan rate (Log *υ*).

Nyquist plots of $SrTiO_3$@$SrCO_3$ and N doped $SrTiO_3$@$SrCO_3$ electrodes, obtained using the electrodes as working electrodes in an electrolyte solution of $K_3Fe(CN)_6$ (0.05 mol L^{-1}) in the dark.

There is a similarity of the Nyquist plots of both electrodes ($SrTiO_3$@$SrCO_3$ and N doped $SrTiO_3$@$SrCO_3$), revealing one semicircle in high-frequency range for both electrodes from the charge-transfer process, and the modified Randles equivalent circuit is presented in the inset of Fig. 7. The equivalent circuit allows a good representation of the quasi-reversible electronic transference, characterized in the semiconductor electrodes. The model establishes that the faradaic current resulting from the electronic transfer at the electrode/electrolyte interface is associated with a capacitive element [48–50]. The behavior of the double layer is represented by a constant phase element (C_d). The resistance R_s corresponds to the resistance of the electrolyte, while R_{ct} is the charge transfer resistance from the electrode to the electrolyte [48]. Finally, a diffusion impedance element, or Warburg impedance, Z_W, is added in series with R_{ct} to represent the diffusion of electroactive species in the electrolyte of infinite thickness. The values of the equivalent elements are shown in Table 1.

The appearance of the Nyquist plot is associated with the transport of oxygen ions by oxygen vacancies, similar with results presented by [50,51]. It can be seen that R_s is similar to both electrodes (Table 2). However, R_{ct} for the electrode is smaller (1.69×10^6 Ω) than those of undoped one (1.79×10^6 Ω), indicating that the doping process can effectively increase the electrical conductivity of the N-doped $SrTiO_3$@$SrCO_3$ electrode. These data demonstrates that N doping facilitates the oxygen ions transport by oxygen vacancies, enabling the increase in electrical conductivity of the N-doped $SrTiO_3$@$SrCO_3$ electrode.

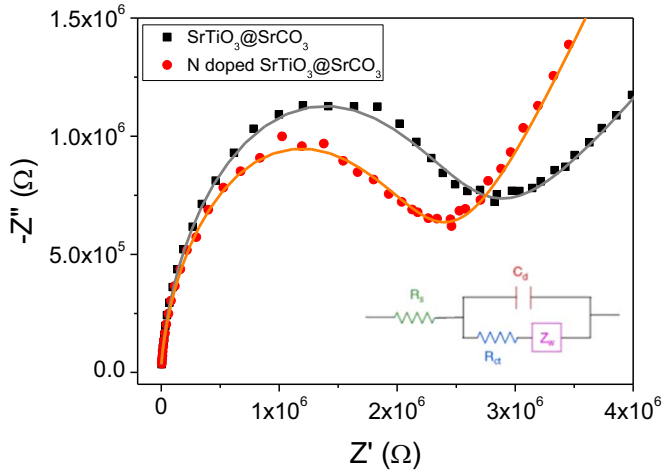

Fig. 7. Electrochemical impedance spectra of $SrTiO_3$@$SrCO_3$ and N doped $SrTiO_3$@$SrCO_3$.

3.5. I-V characteristic of thin film composite electrodes

As the $SrTiO_3$ thin film electrode was characterized with the best number of layers and geometric area, the N-doped $SrTiO_3$@$SrCO_3$ thin film electrode was constructed with the same condition. *I-V* relation of thin film electrodes in the dark and under UV-C illumination was obtained by differential pulse voltammetry to continue the characterization of the photoelectrodes and determine the characteristic differences between them. The $SrTiO_3$@$SrCO_3$ and N doped $SrTiO_3$@$SrCO_3$ thin film photoelectrodes were illuminated with UV-C light (Fig. 8) to determine the differences in energy bands produced by the doping process. Semiconductor photoelectrodes under UV-C illumination absorb the energy of photons, resulting in excited charge carriers (electrons and holes) in the conduction and valence energy bands.

The process of doping *n*-type semiconductors with N atoms creates energy inter-band levels between conduction and valence bands. However, the principal characteristic of N-doping is inter-band energy level creation near to the valence band; i.e., inter-band energy levels created by holes. As the holes are the minor charge carriers in *n*-type semiconductors, the photoelectrode illumination presents an important modification of behavior that is more pronounced in the doped photoelectrode (Fig. 8B) than the undoped photoelectrode (Fig. 8A). UV-C illumination causes an increase in current of roughly 1.28 μA for the $SrTiO_3$@$SrCO_3$ photoelectrode (35.54 μA to 36.82 μA), whereas, for the N-doped $SrTiO_3$@$SrCO_3$ photoelectrode, the increase is 5.07 μA (38.23 μA to 43.30 μA). Furthermore, the results corroborate in N-doping process efficiency and confirm that it is possible to identify the essential difference between undoped and doped materials, especially related to energy bands, by electrochemical measurements. Soares et al. [43] employed electrochemical and photoelectrochemical techniques to investigate the electronic energy level modification of N-doping process in TiO_2 nanoparticles. Authors confirm the photoelectrochemical results with theoretical calculations, proving that photoelectrochemical measurements are useful to investigate the anion doping in semiconductor materials. This result is of particular significance since previous optical analyses for energy band determination of $SrTiO_3$ presented

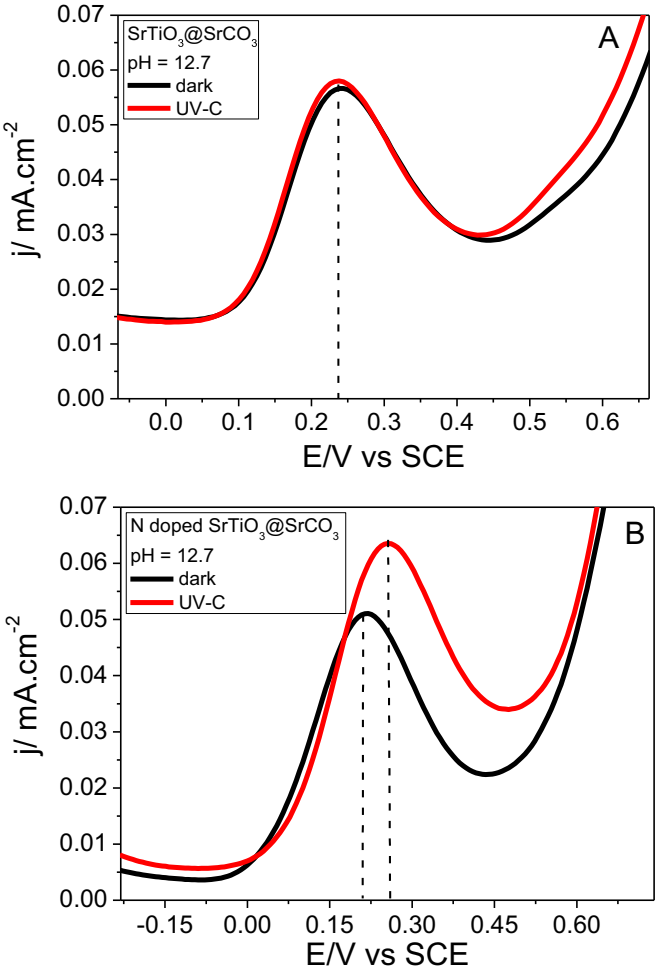

Fig. 8. Differential pulse of $SrTiO_3$@$SrCO_3$ (A) and N doped $SrTiO_3$@$SrCO_3$ (B) photoelectrodes in a solution of $Na_2S{\cdot}9H_2O$ (0.45 M) + K_2SO_4 (0.15 M), at pH = 12.7, with a Pt counter-electrode and ECS reference, in the dark and under UV-C light.

in the literature [33,36] did not clearly detect differences between the undoped and doped material.

The strontium titanate semiconducting materials reported in literature exhibit nonlinear current-voltage (I-V) behavior [52,53]. Devices that show such behavior enable to provide excellent transient suppression performance. The main goal to create a varistor device is to protect electronic devices due to the impressive voltage transient (overvoltage) or electrostatic discharge. The symmetrical, sharp breakdown properties shown in Fig. 9 for electrodes characterize a varistor performance. $SrTiO_3$ varistor is constructed through a mixture of strontium oxide with the small amount of dopant or another oxide, such as PbO, Bi_2O_3, B_2O_3, CoO [52,54]. The synthesis process enables the grain boundary properties to control, better described as a series-parallel arrangement of semiconducting diodes. Defects localized in grain boundaries trap electrons, forming a space charge depletion layer in semiconductor grain close to the grain boundaries. The depletion layer prevents the charge carriers free flow, promoting a low voltage insulating behavior.

Table 2
Nyquist plot results for Randles equivalent circuit of $SrTiO_3$@$SrCO_3$ and N-doped $SrTiO_3$@$SrCO_3$.

Electrodes	R_s (10^3 Ω)	$C_{d1\text{-}T}$ (10^{-11} F)	$C_{d1\text{-}P}$ (F)	R_{ct} (10^6 Ω)	$Z_{Wo1\text{-}R}$ (10^6)	$Z_{Wo1\text{-}T}$ (10^{-2})	$Z_{Wo1\text{-}P}$
$SrTiO_3$@$SrCO_3$	4.00	1.65	0.92	1.79	1.68	0.17	0.18
N doped $SrTiO_3$@$SrCO_3$	4.00	1.66	0.91	1.69	2.10	0.36	0.27

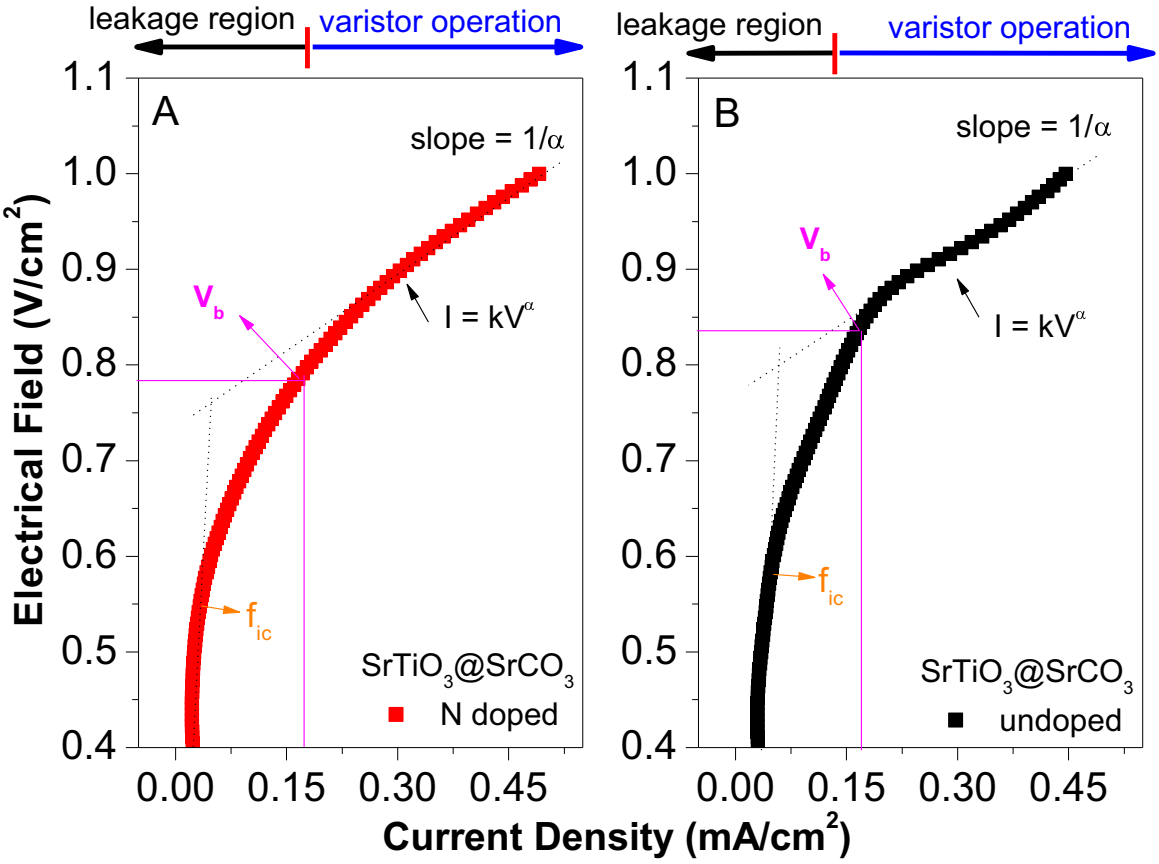

Fig. 9. I–V characteristics of N doped $SrTiO_3$@$SrCO_3$(A) and $SrTiO_3$@$SrCO_3$ (B) electrodes in a solution of $Na_2S{\cdot}9H_2O$ (0.45 M) + K_2SO_4 (0.15 M), at pH = 12.7, with a Pt counter-electrode and ECS reference.

Table 3
Leakage current (f_{ic}), breakdown voltage (V_b) defined in 0.17 mA/cm^2, and, the nonlinear coefficient (α) obtained in the range of 0.15–0.5 mA/cm^2 based in Fig. 9 for $SrTiO_3$@$SrCO_3$ and N doped $SrTiO_3$@$SrCO_3$ composite electrode.

	V_b (V)	f_{ic} (μA)	α
$SrTiO_3$@$SrCO_3$	0.784	37.8	1.504
N doped $SrTiO_3$@$SrCO_3$	0.837	50.9	1.779

Leakage current (f_{ic}) is a very important characteristic in ceramic varistor as it controls stability during its lifetime. From Fig. 9, the leakage current was calculated at 70% of the electric field breakdown (breakdown voltage (V_b)), which is another varistor characteristic and is defined by the average number of electric barriers (Table 3). V_b was extracted when the current density in the varistor was 0.17 mA/cm^2, and, finally, the nonlinear coefficient (α) was obtained in the current range 0.15–0.5 mA/cm^2. Fig. 9 shows how each parameter was obtained and Table 3 presents parameters values. For $SrTiO_3$@$SrCO_3$ composite electrodes, the N doping affects V_b, f_{ic}, and α illustrating one more time that the doping process was effective and electrochemical techniques could be useful in illustrating the difference between undoped and doped material. Values presented in Table 3 differ from those presented in the literature for the system used in high-voltage protection [52,53]. However, leakage current values are similar with those reported for low-voltage protection system [54], confirming that $SrTiO_3$@$SrCO_3$ varistor, doped or undoped with N, is a potential candidate to low-voltage protection system.

4. Conclusion

Some semiconductors do not show significant variation after doping when characterized by traditional techniques, such as diffusive reflectance spectroscopy. Electrochemical characterization confirmed a change in the energy band of a photoelectrode after doping, in a semiconductor material for which doped and undoped samples show similar results when analyzed by traditional techniques, such as DRS and XRD. The thin films were observed by FESEM/SEM, and its deposition parameters were evaluated electrochemically presenting an increase in photo-response with electrode surface area. The charge transfer resistance of the photoelectrode surface was decreased by the doping of particles, and the charge transfer rate increased N-doped $SrTiO_3$@$SrCO_3$ thin film electrodes present greater photocurrent under UV-C illumination. Furthermore, the results corroborate the efficiency of N-doping and confirm that it is possible to identify the essential difference between undoped and doped materials by electrochemical measurements. $SrTiO_3$@$SrCO_3$ composite electrodes show important characteristics which could be classified as a potential candidate in varistor uses, especially in the low-voltage protection system. Electrochemical characterization measurements present distinct results for the undoped and the doped materials, thus confirm the efficiency of N-doping electrochemical characterization.

Ethical statement and conflicts of interest

The authors confirm that agree with all items specified by this Journal about ethical responsibilities of Committee on Publication Ethics (COPE). The authors declare that there are no conflicts of interest regarding the publication of this article.

Acknowledgment

We appreciate the financial support from CNPq (402287/2013-4), SISNANO/MCTI, FINEP, Fapesp (2015/04511-5; 2013/07296-2) and Embrapa AgroNano research network.

Appendix B. Supplementary material

Supplementary data associated with this article can be found in the online version at doi:10.1016/j.ceramint.2017.06.003.

References

[1] A.W. Bott, Electrochemistry of semiconductors, Curr. Sep. 17 (1998) 87–91.
[2] Y.Y. Mi, Z. Yu, S.J. Wang, X.Y. Gao, A.T.S. Wee, C.K. Ong, C.H.A. Huan, Thermal stability of nitrogen-doped $SrTiO_3$ films: electronic and optical properties studies, J. Appl. Phys. 101 (2007) 63708. http://dx.doi.org/10.1063/1.2713350.
[3] P. Reunchan, S. Ouyang, N. Umezawa, H. Xu, Y. Zhang, J. Ye, Theoretical design of highly active $SrTiO_3$-based photocatalysts by a codoping scheme towards solar energy utilization for hydrogen production, J. Mater. Chem. A. 1 (2013) 4221. http://dx.doi.org/10.1039/c2ta00450j.
[4] A.M. Bakhshayesh, N. Bakhshayesh, Materials science in semiconductor processing enhanced short circuit current density of dye-sensitized solar cells aided by Sr, V co-doped TiO_2 particles, Mater. Sci. Semicond. Process. 41 (2016) 92–101. http://dx.doi.org/10.1016/j.mssp.2015.08.030.
[5] C. Zhang, Y. Jia, Y. Jing, Y. Yao, J. Ma, J. Sun, Effect of non-metal elements (B, C, N, F, P, S) mono-doping as anions on electronic structure of $SrTiO_3$, Comput. Mater. Sci. 79 (2013) 69–74. http://dx.doi.org/10.1016/j.commatsci.2013.06.009.
[6] T. Puangpetch, T. Sreethawong, S. Yoshikawa, S. Chavadej, Synthesis and photocatalytic activity in methyl orange degradation of mesoporous-assembled SrTiO3 nanocrystals prepared by sol–gel method with the aid of structure-directing surfactant, J. Mol. Catal. A Chem. 287 (2008) 70–79. http://dx.doi.org/10.1016/j.molcata.2008.02.027.
[7] Y.Y. Mi, S.J. Wang, J.W. Chai, J.S. Pan, C.H.A. Huan, Y.P. Feng, C.K. Ong, Effect of nitrogen doping on optical properties and electronic structures of $SrTiO_3$ films, Appl. Phys. Lett. 89 (2006) 231922. http://dx.doi.org/10.1063/1.2403181.
[8] W. Luo, W. Duan, S. Louie, M. Cohen, Structural and electronic properties of n-doped and p-doped $SrTiO_3$, Phys. Rev. B 70 (2004) 214109. http://dx.doi.org/10.1103/PhysRevB.70.214109.
[9] V. Manthina, J.P. Correa Baena, G. Liu, A.G. Agrios, ZnO–TiO_2 nanocomposite films for high light harvesting efficiency and fast electron transport in dye-sensitized solar cells, J. Phys. Chem. C 116 (2012) 23864–23870. http://dx.doi.org/10.1021/jp304622d.
[10] B. Tang, G. Hu, Two kinds of graphene-based composites for photoanode applying in dye-sensitized solar cell, J. Power Sources 220 (2012) 95–102. http://dx.doi.org/10.1016/j.jpowsour.2012.07.093.
[11] J. Durantini, P.P. Boix, M. Gervaldo, G.M. Morales, L. Otero, J. Bisquert, E.M. Barea, Photocurrent enhancement in dye-sensitized photovoltaic devices with titania–graphene composite electrodes, J. Electroanal. Chem. 683 (2012) 43–46. http://dx.doi.org/10.1016/j.jelechem.2012.07.032.
[12] S. Yin, X. Wang, Z. Mou, Y. Wu, H. Huang, M. Zhu, Y. Du, P. Yang, Synergistic contributions by decreasing overpotential and enhancing charge-transfer in a-Fe_2O_3 / Mn_3O_4 / graphene catalysts with heterostructures for photocatalytic water oxidation, Phys. Chem. Chem. Phys. Phys. Chem. Chem. Phys. 16 (2014) 11289–11296. http://dx.doi.org/10.1039/c4cp00384e.
[13] K.T.G. Carvalho, A.E. Nogueira, O.F. Lopes, G. Byzynski, C. Ribeiro, Enhanced photocatalytic activity of g-C_3N_4/Nb_2O_5 heterostructures on degradation of organic pollutants under visible and ultraviolet irradiation, Appl. Catal. A Gen. Submitt. (2015). http://dx.doi.org/10.1007/s13398-014-0173-7.2.
[14] I.A. de Castro, W. Avansi, C. Ribeiro, WO_3/TiO_2 heterostructures tailored by the oriented attachment mechanism: insights from their photocatalytic properties, CrystEngComm 16 (2014) 1514. http://dx.doi.org/10.1039/c3ce41668b.
[15] X.-J. Lv, S. Zhou, X. Huang, C. Wang, W.-F. Fu, Photocatalytic overall water splitting promoted by SnOx–$NiGa_2O_4$ photocatalysts, Appl. Catal. B Environ. 182 (2016) 220–228. http://dx.doi.org/10.1016/j.apcatb.2015.09.032.
[16] I.A. Castro, G. Byzynski, M. Dawson, C. Ribeiro, Chemistry charge transfer mechanism of WO_3 / TiO_2 heterostructure for photoelectrochemical water splitting, J. Photochem. Photobiol. A Chem. 339 (2017) 95–102. http://dx.doi.org/10.1016/j.jphotochem.2017.02.024.
[17] Y. Liu, G. Li, R. Mi, C. Deng, P. Gao, An environment-benign method for the synthesis of p-NiO/n-ZnO heterostructure with excellent performance for gas sensing and photocatalysis, Sens. Actuators B Chem. 191 (2014) 537–544. http://dx.doi.org/10.1016/j.snb.2013.10.068.
[18] Z. Ni, Y. Sun, Y. Zhang, F. Dong, Fabrication, modification and application of $(BiO)_2CO_3$-based photocatalysts: a review, Appl. Surf. Sci. 365 (2016) 314–335. http://dx.doi.org/10.1016/j.apsusc.2015.12.231.
[19] Y.-L.W.Y.-L. Wang, F.R.F. Ren, H.S. Kim, D.P. Norton, S.J. Pearton, Materials and process development for ZnMgO/ZnO light-emitting diodes, IEEE J. Sel. Top. Quantum Electron. 14 (2008) 1048–1052. http://dx.doi.org/10.1109/JSTQE.2008.919736.
[20] C. Khare, K. Sliozberg, R. Meyer, A. Savan, W. Schuhmann, A. Ludwig, Layered WO_3 / TiO_2 nanostructures with enhanced photocurrent densities, Int. J. Hydrog. Energy 38 (2013) 15954–15964. http://dx.doi.org/10.1016/j.ijhydene.2013.09.142.
[21] J. Zhou, L. Yin, H. Li, Z. Liu, J. Wang, K. Duan, S. Qu, J. Weng, B. Feng, Heterojunction of $SrTiO_3$ / TiO_2 nanotubes with dominant (001) facets: synthesis, formation mechanism and photoelectrochemical properties, Mater. Sci. Semicond. Process. 40 (2015) 107–116. http://dx.doi.org/10.1016/j.mssp.2015.06.023.
[22] A. Márquez-Herrera, V.M. Ovando-Medina, B.E. Castillo-Reyes, M. Meléndez-Lira, M. Zapata-Torres, N. Saldaña, A novel synthesis of $SrCO_3$–$SrTiO_3$ nanocomposites with high photocatalytic activity, J. Nanopart. Res. 16 (2014). http://dx.doi.org/10.1007/s11051-014-2804-5.
[23] X. Pan, X. Chen, Z. Yi, Photocatalytic oxidation of methane over $SrCO_3$ decorated $SrTiO_3$ nanocatalysts via a synergistic effect, Phys. Chem. Chem. Phys. 18 (2016) 31341–31976. http://dx.doi.org/10.1039/c6cp04604e.
[24] G. Branković, Z. Branković, J.A. Varela, E. Longo, Strontium titanate films prepared by spray pyrolysis, J. Eur. Ceram. Soc. 24 (2004) 989–991. http://dx.doi.org/10.1016/S0955-2219(03)00459-X.
[25] M. Vehkamäki, T. Hänninen, M. Ritala, M. Leskelä, T. Sajavaara, E. Rauhala, J. Keinonen, Atomic layer deposition of $SrTiO_3$ thin films from a novel strontium precursor- Strontium-bis(*tri*-isopropylcyclopentadienyl), Chem. Vap. Depos. 7 (2001) 75–80. http://dx.doi.org/10.1002/1521-3862(200103)7:2 < 75::AID-CVDE75 > 3.0.CO;2-B.
[26] S. Rentrop, T. Moebus, B. Abendroth, R. Strohmeyer, A. Schmid, T. Weling, J. Hanzig, F. Hanzig, H. Stöcker, D.C. Meyer, Atomic layer deposition of strontium titanate films from Sr($iPr_3Cp)_2$, Ti[$N(CH_3)_2]_4$ and H_2O, Thin Solid Films. 550 (2014) 53–58. http://dx.doi.org/10.1016/j.tsf.2013.10.043.
[27] G.B. Soares, C.M.P. Vaz, C. Ribeiro, I. Hermans, Insight into the photocatalytical activity of TiO_2 nanoparticles through the electrochemical characterization of carbon paste electrodes, Electrocatalysis 6 (2015) 92–101. http://dx.doi.org/10.1007/s12678-014-0223-0.
[28] S.C. Erwin, L. Zu, M.I. Haftel, A.L. Efros, T.A. Kennedy, D.J. Norris, Doping semiconductor nanocrystals, Nature 436 (2005) 91–94. http://dx.doi.org/10.1038/nature03832.
[29] M. Anas, D.S. Han, K. Mahmoud, H. Park, A. Abdel-Wahab, Photocatalytic degradation of organic dye using titanium dioxide modified with metal and non-metal deposition, Mater. Sci. Semicond. Process. 41 (2016) 209–218. http://dx.doi.org/10.1016/j.mssp.2015.08.041.
[30] H.B. Jalali, L. Trabzon, Structural and optical properties of nitrogen-iron co-doped titanium dioxide films prepared via sol-gel dip-coating: effect of urea and iron nitrate concentration in the sol, Materwiss. Werksttech. 47 (2016) 657–664. http://dx.doi.org/10.1002/mawe.201600506.
[31] Y. Liu, L. Xie, Y.Y. Li, R. Yang, J. Qu, Y.Y. Li, X. Li, Synthesis and high photocatalytic hydrogen production of SrTiO3 nanoparticles from water splitting under UV irradiation, J. Power Sources 183 (2008) 701–707. http://dx.doi.org/10.1016/j.jpowsour.2008.05.057.
[32] P. Xiang, X. Li, H. Wang, G. Liu, T. Shu, Z. Zhou, Z. Ku, Y. Rong, M. Xu, L. Liu, M. Hu, Y. Yang, W. Chen, T. Liu, M. Zhang, H. Han, Mesoporous nitrogen-doped TiO_2 sphere applied for quasi-solid-state dye-sensitized solar cell, Nanoscale Res. Lett. 6 (2011) 1–5. http://dx.doi.org/10.1186/1556-276X-6-606.
[33] N. Nuraje, Y. Lei, A. Belcher, Virus-templated visible spectrum active perovskite photocatalyst, Catal. Commun. 44 (2014) 68–72. http://dx.doi.org/10.1016/j.catcom.2013.08.001.
[34] A. Uedono, M. Kiyohara, K. Shimoyama, K. Yamabe, T. Ohdaira, R. Suzuki, T. Mikado, Defects introduced into $SrTiO_3$ by auto-feeding epitaxy studied using positron annihilation technique, Mater. Sci. Semicond. Process. 6 (2003) 367–369. http://dx.doi.org/10.1016/j.mssp.2003.07.010.
[35] M. Usman, S. Mendiratta, S. Batjargal, G. Haider, M. Hayashi, N. Rao Gade, J.-W. Chen, Y.-F. Chen, K.-L. Lu, Semiconductor behavior of a three-dimensional strontium-based metal-organic framework, ACS Appl. Mater. Interfaces 7 (2015) 22767–22774. http://dx.doi.org/10.1021/acsami.5b07228.
[36] X.X. Liao, H.Q. Wang, J.C. Zheng, Tuning the structural, electronic, and magnetic properties of strontium titanate through atomic design: a comparison between oxygen vacancies and nitrogen doping, J. Am. Ceram. Soc. 96 (2013) 538–543. http://dx.doi.org/10.1111/jace.12072.
[37] G.B. Soares, B. Bravin, C.M.P. Vaz, C. Ribeiro, Facile synthesis of N-doped TiO_2 nanoparticles by a modified polymeric precursor method and its photocatalytic properties, Appl. Catal. B Environ. 106 (2011) 287–294. http://dx.doi.org/10.1016/j.apcatb.2011.05.018.
[38] S. Yoon, A.E. Maegli, L. Karvonen, S.K. Matam, A. Shkabko, S. Riegg, T. Großmann, S.G. Ebbinghaus, S. Pokrant, A. Weidenkaff, Journal of solid state chemistry bandgap tuning in SrTi (N,O, $F)_3$ by anionic-lattice variation, J. Solid State Chem. 206 (2013) 226–232. http://dx.doi.org/10.1016/j.jssc.2013.08.001.
[39] W. Wei, Y. Dai, H. Jin, B. Huang, Density functional characterization of the electronic structure and optical properties of Cr-doped $SrTiO_3$, J. Phys. D. Appl. Phys. 42 (2009) 55401. http://dx.doi.org/10.1088/0022-3727/42/5/055401.
[40] M. Dawson, G.B. Soares, C. Ribeiro, Influence of calcination parameters on the synthesis of N-doped TiO_2 by the polymeric precursors method, J. Solid State Chem. 215 (2014) 211–218. http://dx.doi.org/10.1016/j.jssc.2014.03.044.
[41] D. Ramírez-Ortega, P. Acevedo-Peña, F. Tzompantzi, R. Arroyo, F. González, I. González, Energetic states in SnO_2–TiO_2 structures and their impact on interfacial charge transfer process, J. Mater. Sci. (2016). http://dx.doi.org/10.1007/s10853-016-0328-3.
[42] G.B. Soares, W.T.L. da Silva, C.M.P. Vaz, Graphite-polyurethane composite electrode for the electroanalytical determination of herbicide diuron in soil solutions, Sens. Lett. 9 (2011) 1786–1793. http://dx.doi.org/10.1166/sl.2011.1712.
[43] G.B. Soares, R.A.P. Ribeiro, S.R. de Lazaro, C. Ribeiro, Photoelectrochemical and

theoretical investigation of the photocatalytic activity of TiO_2:N, RSC Adv. 6 (2016) 89687–89698. http://dx.doi.org/10.1039/C6RA15825K.
[44] A.J. Bard, L.R. Faulkner, N. York, C. @bullet, W. Brisbane, S.E. Toronto, ELECTROCHEMICAL METHODS Fundamentals and Applications, 1944. doi:10.1016/B978-0-12-381373-2.00056-9.
[45] D. Laser, a.J. Bard, Semiconductor electrodes. IV. Electrochemical behavior of n- and p-type silicon electrodes in acetonitrile solutions, J. Phys. Chem. 80 (1976) 459–466. http://dx.doi.org/10.1021/j100546a008.
[46] H.V.M. Hamelers, A. ter Heijne, N. Stein, R.A. Rozendal, C.J.N. Buisman, Butler-Volmer-Monod model for describing bio-anode polarization curves, Bioresour. Technol. 102 (2011) 381–387. http://dx.doi.org/10.1016/j.biortech.2010.06.156.
[47] K. Rajeshwar, Fundamentals of semiconductors electrochemistry and photoelectrochemistry, Encycl. Electrochem. (2007) 1–51. http://dx.doi.org/10.1002/9783527610426.bard060001.
[48] P.R. Bueno, J.A. Varela, E. Longo, SnO_2, ZnO and related polycrystalline compound semiconductors: an overview and review on the voltage-dependent resistance (non-ohmic) feature, J. Eur. Ceram. Soc. 28 (2008) 505–529. http://dx.doi.org/10.1016/j.jeurceramsoc.2007.06.011.
[49] G. Gregori, S. Heinze, P. Lupetin, H.U. Habermeier, J. Maier, Seebeck coefficient and electrical conductivity of mesoscopic nanocrystalline $SrTiO_3$, J. Mater. Sci. 48 (2013) 2790–2796. http://dx.doi.org/10.1007/s10853-012-6894-0.
[50] L. Dai, L. Wu, H. Li, H. Hu, Y. Zhuang, K. Liu, Evidence of the pressure-induced conductivity switching of yttrium-doped $SrTiO_3$, J. Phys. Condens. Matter 28 (2016) 475501. http://dx.doi.org/10.1088/0953-8984/28/47/475501.
[51] E. Drożdż, A. Łącz, A. Koleżyński, A. Mikuła, K. Mars, Experimental and theoretical studies of structural and electrical properties of highly porous Sr_1-xYxTiO_3, Solid State Ion. 302 (2017) 173–179. http://dx.doi.org/10.1016/j.ssi.2016.11.014.
[52] J.Q. Sun, W.P. Chen, W. Xiang, W.C. You, Y. Zhuang, H.L.W. Chan, Degradation of $SrTiO_3$-based ceramic varistors induced by water and ac voltages, Ceram. Int. 33 (2007) 1137–1140. http://dx.doi.org/10.1016/j.ceramint.2006.03.005.
[53] J. Li, S. Li, M.A. Alim, The effect of reducing atmosphere on the $SrTiO_3$ based varistor-capacitor materials, (2006) pp. 503–508. doi:10.1007/s10854-006-7469-0.
[54] M. Cilense, M.A. Ramirez, C.R. Foschini, D.R. Leite, Effect of Seed Addition on SnO_2 -Based Varistors for Low Voltage Application, 530 (2013) pp. 524–530. doi:10.1111/jace.12064.